# Improved CE/SE scheme with particle level set method for numerical simulation of spall fracture due to high-velocity impact

Qianyi Chen [a,b], Jingtao Wang [a], Kaixin Liu [a,b,*]

[a] LTCS and Department of Mechanics and Aerospace Engineering, College of Engineering, Peking University, 100871 Beijing, China
[b] Center for Applied Physics and Technology, Peking University, 100871 Beijing, China

## ARTICLE INFO

## ABSTRACT

In the present paper, an Eulerian scheme combined with the hybrid particle level set method for numerical simulation of spall fracture due to high-velocity impact is proposed. An axisymmetric framework is established, based on an improved CE/SE scheme, to solve the high-velocity impact problems with large deformations, high strain rates and spall fractures. The hybrid particle level set method is adopted for tracking material interfaces and describing the formation and propagation of a crack. A novel representation of crack by level set is proposed. Numerical simulations are carried out and compared to the corresponding experimental results. The numerical results are in good agreement with the experimental data. The edge effects are reproduced and the decrease of scab thickness with increase in impact velocity is observed owing to the numerical analysis. It is proved that our computational technique is feasible and reliable for analyzing the spall fracture.

© 2010 Elsevier Inc. All rights reserved.

## 1. Introduction

Spall fracture happens mainly in the field of high-velocity impact. It is a kind of dynamic fracture that occurs inside a material when two decompression waves interact and produce enough tension to cause damage. The process of the spall fracture is considered as a sequence of nucleation, growth and coalescence of microscopic voids or cracks [1]. The classical plate-impact experiment is usually used to study the mechanisms of the spall fracture in the laboratories [2–4].

Numerical analysis plays an important role in the study of the spall fracture. It enables the researchers to obtain the information such as pressure, strain rate and porosity evolution inside the target during the tests, which cannot be captured during the experiments. Two kinds of dynamic fracture models for the numerical simulation of the spall, which consider the microvoiding process, are currently popular. They are the void growth (VG) model [5–9] and the nucleation and growth (NAG) model [3,10]. The VG model is a mathematical model of ductile holes growth under the application of a mean tensile stress. The NAG model considers more physical details including the nucleation and the growth processes. Eftis et al. [11] performed numerical simulations, by their own constitutive-microdamage equations, for describing the impact of spherical projectiles with rectangular target plates at a speed of 6.0 km/s. Three ratios of the projectile diameter to the target thickness were chosen, and different damage features were presented in the simulations. Ikkurthi and Chaturvedi [12] adopted four damage models for the simulations of the spall fracture in metal plates. The best match with the experiments was obtained by the VG model. Several physical phenomena such as the edge effects were also studied. Czarnota et al. [10] carried out the finite element simulations of the plate-impact tests based on the model proposed by themselves and compared the

---

* Corresponding author at: LTCS and Department of Mechanics and Aerospace Engineering, College of Engineering, Peking University, 100871 Beijing, China. Tel.: +86 10 62765844; fax: +86 10 62751812.

E-mail addresses: chenqy@pku.edu.cn (Q. Chen), wang@imes.mavt.ethz.ch (J. Wang), kliu@pku.edu.cn (K. Liu).

numerical results to the experiments on tantalum. An increase of the spall strength was observed with higher shock intensities in the simulations.

Meanwhile, in the community of computational mechanics, a number of hydrocodes by which high-velocity impact calculations are performed have appeared in the last 30 years. These codes can be classified basically into three kinds: Lagrangian formulation (such as TOODY, EPIC and DYNA), Eulerian formulation (such as CSQ, CTH and MESA) and arbitrary Lagrangian–Eulerian (ALE) formulation (such as CAVEAT and SALE) [13]. Anderson [14] summarized the advantages and disadvantages of both Lagrangian and Eulerian descriptions. Johnson and Anderson [15] gave a review of the development of hydrocodes from a historical point of view. Benson [13] published a comprehensive survey which describes in detail the algorithms that are currently used in the modern hydrocodes. Lagrangian schemes work well at multimaterial interfaces, but suffer from their own troubles in problems with large deformations. The extreme case is that the simulation fails when a grid cell folds over itself. The way to avoid computational failure is to remesh the scheme where large distortion appears, which decreases the accuracy of the solution and the computational efficiency. Although the ALE method allows the mesh to move, the adaptive remeshing technologies are also required in regions with large deformations. Eulerian codes, however, allowing the boundaries to flow through a fixed mesh while computing the flow field on the fixed mesh, can solve arbitrarily large distortions. Coupled with an appropriate interface capturing algorithm, the Eulerian formulation will be quite attractive to high-velocity impact problems with large deformations.

Traditional Eulerian codes, mainly using first-order difference schemes and the von Neumann artificial viscosity, have low accuracy and cannot capture strong shock waves very well. In recent years, some researchers have applied the high-resolution techniques in the field of modern computational fluid dynamics (CFD) to the elastic–plastic flow problems. Benson [16] proposed an Eulerian formulation which is of the Lagrangian-plus-remap type and applied it to impact problems involving penetration and fracture. Cooper et al. [17] extended the Lagrangian-plus-remap method to simulate the dynamic void collapse in copper to study hot spot formation and jetting. Udaykumar et al. [18] presented a technique for the numerical simulation of high-speed multimaterial impact. The computations were performed on a fixed Cartesian mesh by casting the equations governing material deformation in Eulerian conservation law form. A high-order accurate ENO scheme was adopted along with the interface tracking technique to evolve sharp boundaries. After that, Tran and Udaykumar [19] updated their methodology by substituting the hybrid particle level set method [20] for the interface tracking algorithm adopted in the previous paper. These efforts have not only improved the accuracy of the numerical results for the problems of elastic–plastic flow, but also shown a remarkable direction in the field of computational mechanics.

The level set method (LSM), as mentioned above, was first devised by Osher and Sethian [21] as a simple and versatile method for tracking the boundary of a moving interface. The principle of this method is to describe an interface by the zero level set of a smooth function, called the level set function, and to update this function with Hamilton–Jacobi equations knowing the speed of the interface. The development and the application of the LSM were discussed in a review article by Osher and Fedkiw [22]. Enright et al. [20] improved the mass conservation properties of the LSM by using Lagrangian marker particles to rebuild the level set in regions which were being under-resolved. The method proposed by them is called the hybrid particle LSM.

A few years ago, Stolarska et al. [23] introduced the LSM to the field of the numerical simulation of crack propagation in solids. They coupled the LSM with the extended finite element method (FEM) and obtained satisfying results. Lately, Duflot [24] has reviewed in detail the update techniques of the crack representation by level set functions and proposed several new techniques. In these methods, a crack is an open curve (an open surface in three dimensions) that grows from its tip (its front in three dimensions), and two level set functions are necessary to represent a crack. When it comes to the spall fracture, however, this kind of crack representation becomes inappropriate. The crack appearing in the spall fracture opens wide with the motion of the scab. If the crack is modeled as a curve, the scab will never separate. In addition, it is unreasonable to put an initial crack in the target plate before simulation. In the present paper, a novel representation of crack by level set is proposed. The crack is represented as a two-dimensional narrow region which can be in any shape according to the specific problem. Free surfaces are created due to the crack.

The space–time conservation element and solution element (CE/SE) method, originally devised by Chang [25,26], is a novel numerical scheme for solving hyperbolic conservation laws. It has several attractive features: (a) being mathematically simple; (b) a unified treatment of both space and time and enforcement of flux conservation in both space and time; (c) very little or almost no numerical dissipation; (d) the lack of directional splitting for flows in multiple spatial dimensions, resulting in a truly multidimensional scheme. The features mentioned above make the method substantially different from traditional well-established methods such as the finite difference and the finite volume methods. The CE/SE method has been generalized to high-order accuracy [27] and has reached a great success in the field of CFD [28–34]. Loh et al. [28] tested the CE/SE scheme for several problems ranging from linear acoustic waves to strongly nonlinear phenomena, with special emphasis on mixing-layer instability, and obtained satisfying numerical results. Wang et al. [32] simulated the detonation propagations with detailed chemical reaction models in a second-order accuracy CE/SE method. Recently, Wang et al. [35] have proposed an improved CE/SE scheme and extended it to the community of high-speed impact dynamics in solids. They have simulated two classical impact problems, Taylor bar impact and penetration. The comparisons with the experimental data and the results from other literature have proved the reliability of the computational technique developed by them.

The present paper extends the methodology proposed by Wang et al. [35] to simulate the spall fracture by introducing the idea of "element erosion" from the FEM. We apply the improved CE/SE scheme [35] to the high-velocity impact problems containing elastic–plastic flows, high strain rates and spall fractures in an axisymmetric framework. The Steinberg–Guinan

(SG) constitutive model [36] and the Mie-Gruneisen (MG) equation of state (EOS) [37] are used to describe the target plate. The hybrid particle LSM [20] is adopted for capturing material interfaces and the physical boundary conditions are applied at the interfaces. We investigate the free boundary conditions and the contact boundary conditions in detail on the stress, velocity, density and internal energy. The VG model [5] is introduced to the codes to monitor the void volume fraction (VVF) of each element. The element is deleted, when its VVF reaches a critical value, to express the formation and propagation of a crack. Simulations of plate-impact experiments performed by Russian scientists [38] are presented. Our numerical results are in good agreement with the experimental observations described in the Russian spall database, which proves the feasibility and reliability of our computational technique.

Within the authors' scope of knowledge, it is the first time to apply the LSM to describe the spall fracture. Since the Eulerian formulation can solve arbitrarily large distortions and the LSM has been successfully used for capturing interfaces undergoing extreme topological changes, the methodology presented here has advantages in simulating dynamic fracture such as spall in ductile materials caused by high-velocity or hypervelocity impact.

## 2. Governing equations

Using cylindrical coordinates $(r, z, \theta)$, not considering the effects of heat conducting, thermal diffusion and external forces, we express the Eulerian governing equations for homogenous media in the form of conservation laws [35]. For an axisymmetric problem, as illustrated in Fig. 1, the vector form of the equations can be written as

$$\frac{\partial \mathbf{Q}}{\partial t} + \frac{\partial \mathbf{E}(\mathbf{Q})}{\partial r} + \frac{\partial \mathbf{F}(\mathbf{Q})}{\partial z} = \mathbf{S}(\mathbf{Q}), \tag{1}$$

where $\mathbf{Q}$ is the vector of conservation variables, $\mathbf{E}$ and $\mathbf{F}$ are the conservation flux vectors in the $r$ and the $z$ directions, respectively, and $\mathbf{S}$ is the source term vector. In the Eulerian form, these vectors are:

$$\mathbf{Q} = \begin{bmatrix} \rho \\ \rho u \\ \rho v \\ E \\ s_{rr} \\ s_{zz} \\ s_{\theta\theta} \\ s_{rz} \\ \varepsilon^p \\ T \\ \alpha \end{bmatrix}, \quad \mathbf{E} = \begin{bmatrix} \rho u \\ \rho u^2 - \sigma_{rr} \\ \rho u v - \sigma_{rz} \\ u(E - \sigma_{rr}) - v\sigma_{rz} \\ u s_{rr} \\ u s_{zz} \\ u s_{\theta\theta} \\ u s_{rz} \\ u\varepsilon^p \\ uT \\ u\alpha \end{bmatrix}, \quad \mathbf{F} = \begin{bmatrix} \rho v \\ \rho u v - \sigma_{rz} \\ \rho v^2 - \sigma_{zz} \\ v(E - \sigma_{zz}) - u\sigma_{rz} \\ v s_{rr} \\ v s_{zz} \\ v s_{\theta\theta} \\ v s_{rz} \\ v\varepsilon^p \\ vT \\ v\alpha \end{bmatrix}, \quad \mathbf{S} = \begin{bmatrix} -(1/r)\rho u \\ -(1/r)(\rho u^2 + \sigma_{\theta\theta} - \sigma_{rr}) \\ -(1/r)(\rho u v - \sigma_{rz}) \\ -(1/r)(u(E - \sigma_{rr}) - v\sigma_{rz}) \\ S_{s_{rr}} \\ S_{s_{zz}} \\ S_{s_{\theta\theta}} \\ S_{s_{rz}} \\ S_{\varepsilon^p} \\ S_T \\ S_\alpha \end{bmatrix}, \tag{2}$$

where $\rho$ is the density, $u$ and $v$ are the $r$ and $z$ components of the velocity respectively, $E = \rho I + (1/2)\rho(u^2 + v^2)$ is the total energy per unit volume, $I$ is the internal energy per unit mass, $p$ is the hydrostatic pressure, $\sigma_{rr}, \sigma_{zz}, \sigma_{\theta\theta}$ and $\sigma_{rz}$ are the components of the stress tensor, $s_{rr}, s_{zz}, s_{\theta\theta}$ and $s_{rz}$ are the components of the deviatoric stress tensor, $\varepsilon^p$ is the equivalent plastic strain, $T$ is the temperature affected by plastic work, and $\alpha$ is the variable for the VG model [5] which will be discussed later.

The hydrostatic pressure $p$ reflects the volume deformation. When the solid material is under a condition of high strain rate deformation, we can assume that $p$ is determined by the thermodynamic EOS like fluid. The specific EOS in use here is the MG EOS [37] which is expressed as
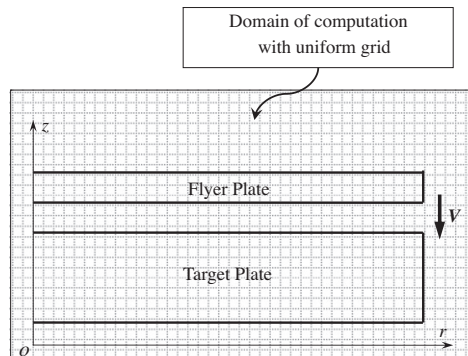


Fig. 1. Computational setup for the study of axisymmetric impact of two metal plates.

$$p = \begin{cases} \dfrac{\rho_0 C_0^2 \mu \left[1 + \left(1 - \frac{\gamma_0}{2}\right)\mu\right]}{[1-(s-1)\mu]^2} + \gamma \rho I & \mu \geqslant 0 \\ \rho_0 C_0^2 \mu + \gamma \rho I & \mu < 0 \end{cases}, \tag{3}$$

where $\mu = \rho/\rho_0 - 1$, $\rho_0$ and $C_0$ are the density and the bulk sound speed at zero pressure, $s$ is the coefficient that relates the shock speed to the particle velocity, $\gamma$ is approximated by $\gamma = \rho_0 \gamma_0/\rho$ and $\gamma_0$ is the Gruneisen parameter.

The deviatoric stress tensor $s_{ij}$ which obeys the Hooke's law in the incremental stress form and the plasticity flow model reflects the shear deformation. In the elastic state, the source terms of $S_{s_{rr}}$, $S_{s_{zz}}$, $S_{s_{\theta\theta}}$ and $S_{s_{rz}}$ in Eq. (2) can be expressed as

$$S_{s_{rr}} = s_{rr}\left(\frac{\partial u}{\partial r} + \frac{\partial v}{\partial z}\right) + 2\Omega_{rz}s_{rz} + 2G\left(\frac{\partial u}{\partial r} - \Phi\right), \tag{4}$$

$$S_{s_{zz}} = s_{zz}\left(\frac{\partial u}{\partial r} + \frac{\partial v}{\partial z}\right) - 2\Omega_{rz}s_{rz} + 2G\left(\frac{\partial v}{\partial z} - \Phi\right), \tag{5}$$

$$S_{s_{\theta\theta}} = s_{\theta\theta}\left(\frac{\partial u}{\partial r} + \frac{\partial v}{\partial z}\right) + 2G\left(\frac{u}{r} - \Phi\right), \tag{6}$$

$$S_{s_{rz}} = s_{rz}\left(\frac{\partial u}{\partial r} + \frac{\partial v}{\partial z}\right) + \Omega_{rz}s_{zz} - \Omega_{rz}s_{rr} + G\left(\frac{\partial u}{\partial z} + \frac{\partial v}{\partial r}\right), \tag{7}$$

where $G$ is the shear modulus, $\Omega_{rz} = \frac{1}{2}\left[\frac{\partial u}{\partial z} - \frac{\partial v}{\partial r}\right]$ is the component of spin tensor and $\Phi = \frac{1}{3}\left(\frac{\partial u}{\partial r} + \frac{u}{r} + \frac{\partial v}{\partial z}\right)$ is the volume strain.

The plastic stress–strain relation is modeled by the von Mises yield criterion and the Prandtl–Reuss flow rule. The von Mises yield condition can be written in terms of the deviatoric stresses as

$$s_{rr}^2 + s_{zz}^2 + s_{\theta\theta}^2 + 2s_{rz}^2 \leqslant \frac{2}{3}\sigma_Y^2, \tag{8}$$

where $\sigma_Y$ is the current yield strength of the material, i.e., the current von Mises flow stress. In our numerical scheme, if the deviatoric stress components calculated from Eq. (1) do not satisfy the yield criterion Eq. (8), they need to be pulled back onto the yield surface. The first correcting scheme was proposed by Willkins [39] in 1964. Recently, Ponthot [40] developed another correcting method which was unified to treat the elasto-plastic and elasto-viscoplastic processes.

The yield stress and the shear modulus of the target plates are determined by the SG constitutive model [36] in the current work. Steinberg and co-workers have produced expressions for the yield stress and the shear modulus as functions of effective plastic strain, pressure and temperature and constants for 14 metals. They have demonstrated that their simulations have reproduced measured stress and free-surface-velocity versus time data for a number of shock wave experiments by this model. The relations for yield stress $Y$ and shear modulus $G$ can be expressed as [36]:

$$Y = Y_0\left\{1 + \left(\frac{Y_p'}{Y_0}\right)\frac{p}{(\rho/\rho_0)^{1/3}} + \left(\frac{G_T'}{G_0}\right)(T - 300)\right\}(1 + \beta\varepsilon)^n, \tag{9}$$

$$G = G_0\left\{1 + \left(\frac{G_p'}{G_0}\right)\frac{p}{(\rho/\rho_0)^{1/3}} + \left(\frac{G_T'}{G_0}\right)(T - 300)\right\}, \tag{10}$$

where $\varepsilon$ is the effective plastic strain. All other parameters in the expressions are material constants. Information about the model in detail is available in Ref. [36]. The flyer plate is described by the Johnson–Cook model [41,42].

The temperature in the SG model reflects the thermal softening effect of the materials. Assuming that the temperature increase of the material is mainly caused by plastic work, the incremental expression of the temperature is

$$\rho C \frac{dT}{dt} = \beta \dot{W}_p, \tag{11}$$

where $C$ is the specific heat, and $\beta$, which is usually taken as 0.9 [43], is the Taylor–Quinney coefficient implying the fraction of mechanical power converting into thermal energy. $\dot{W}_p$ is the rate of plastic work, which is approximated by $\dot{W}_p \approx \dot{\varepsilon}^p\sqrt{(3/2)s_{ij}s_{ij}}$, where $\dot{\varepsilon}^p$ is the equivalent plastic strain rate and defined as

$$\dot{\varepsilon}^p = \sqrt{\frac{2}{3}\dot{D}_{ij}^p\dot{D}_{ij}^p}, \tag{12}$$

where $\dot{D}_{ij}^p$ is the plastic strain rate, the expression of which is discussed in detail in Ref. [40]. According to Eqs. (11) and (12), the source terms of the equivalent plastic strain and the temperature in Eq. (2) can be expressed as

$$S_{\varepsilon^p} = \varepsilon^p\left(\frac{\partial u}{\partial r} + \frac{\partial v}{\partial z}\right) + \sqrt{\frac{2}{3}\dot{D}_{ij}^p\dot{D}_{ij}^p}, \tag{13}$$

$$S_T = T\left(\frac{\partial u}{\partial r} + \frac{\partial v}{\partial z}\right) + \frac{\beta\dot{W}_p}{\rho C}. \tag{14}$$

Ikkurthi and Chaturvedi [12] have studied spallation in impact-loaded metal plates, using four different damage models. The VG model yields the closest match with the experiments according to their work. Hence we choose the VG model in the current work. In the VG model, the presence of voids is expressed in terms of the distension ratio $\alpha$, which is related to the porosity $\phi$ according to $\phi = 1 - 1/\alpha$. In the absence of inertial effects, the rate of change of $\alpha$ is given by

$$\frac{d\alpha}{dt} = 0, \quad \Delta p \geqslant 0,$$ (15)

$$\frac{d\alpha}{dt} = -\frac{(\alpha_0 - 1)^{2/3}}{\eta}\alpha(\alpha - 1)^{1/3}\Delta p, \quad \Delta p < 0,$$ (16)

where $\Delta p$ is the driving stress for void growth as given by

$$\Delta p = \bar{p} + \frac{a_s}{\alpha}\ln\left(\frac{\alpha}{\alpha - 1}\right).$$ (17)

Here $\eta$ is a material parameter, $a_s$ controls the threshold for void growth and $\alpha_0$ provides the initial distension to get the void growth process started. The variable $\bar{p}$ is the mean stress in the porous region containing voids. More information is available in Ref. [5]. Using Eulerian representation, we write the VG model as

$$\frac{\partial\alpha}{\partial t} + \frac{\partial u\alpha}{\partial r} + \frac{\partial v\alpha}{\partial z} = \alpha\left(\frac{\partial u}{\partial r} + \frac{\partial v}{\partial z}\right) - \frac{(\alpha_0 - 1)^{2/3}}{\eta}\alpha(\alpha - 1)^{1/3}\Delta p.$$ (18)

Hence the source term of the distension $\alpha$ in Eq. (2) is

$$S_\alpha = \alpha\left(\frac{\partial u}{\partial r} + \frac{\partial v}{\partial z}\right) - \frac{(\alpha_0 - 1)^{2/3}}{\eta}\alpha(\alpha - 1)^{1/3}\Delta P.$$ (19)

The governing equations presented above can be used to describe high-velocity impact problems with large deformations and high strain rates. We will solve the equations in a newly developed high-resolution scheme developed by us.

## 3. The improved CE/SE scheme

According to the physical conservation laws, the flux conservation is required not only in space but in time. In order to keep the conservation of flux in both space and time, the CE/SE scheme is constructed by the innovative concept of unified treatment of space and time. For problems in two spatial dimensions $(r, z)$, the CE/SE scheme is established in a three-dimensional Euclidean space $E_3$ with coordinates $(r, z, t)$.

The definitions of conservation element (CE) and solution element (SE) are illustrated in Fig. 2. The SE is defined as the vicinity of a mesh point such as point P′ in Fig. 2(a). The physical variables on SE(P′) are approximated by the first-order Taylor's expansions at P′$(r, z, t)$. For example:

$$Q_m(dr, dz, dt)_{P'} = (Q_m)_{P'} + (Q_{mr})_{P'}dr + (Q_{mz})_{P'}dz + (Q_{mt})_{P'}dt,$$ (20)

where $Q_m(dr, dz, dt)$ is a physical variable at point $(r, z, t)$, $dr = r - r_{P'}$, $dz = z - z_{P'}$, $dt = t - t_{P'}$, $(Q_m)_{P'}$ is the value of $Q_m$ at P′, $(Q_{mr})_{P'}$ and $(Q_{mz})_{P'}$ are the spatial derivatives of $Q_m$ at P′, $(Q_{mt})_{P'}$ is the temporal derivative of $Q_m$ at P′.

An SE is divided by the time plane into two CEs which are general hexahedrons as shown in Fig. 2(b). Supposing that the conservation Eq. (1) is satisfied in every CE, its integral form in the CE is

$$\iiint\limits_{V(CE)} \frac{\partial Q}{\partial t} + \frac{\partial E(Q)}{\partial r} + \frac{\partial F(Q)}{\partial z} drdzdt = \iiint\limits_{V(CE)} S(Q)drdzdt.$$ (21)
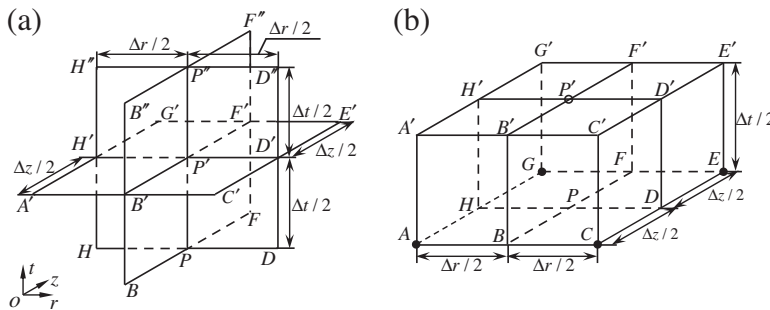


**Fig. 2.** Diagram for the explanation of formation of the CE/SE scheme. Axis $r$ and axis $z$ are spatial coordinates. Axis $t$ represents the temporal variable. (a) Solution element (SE). (b) Conservation element (CE).

According to the Gauss' divergence theorem, the above expression can be rewritten as

$$\oint\limits_{S(V)} \vec{H} \cdot d\vec{s} = \iiint\limits_{V(CE)} S(Q)drdzdt, \quad \vec{H} = (Q, E, F), \quad d\vec{s} = \vec{n}ds, \tag{22}$$

where $S(V)$ is the boundary of the space–time volume CE, $\vec{H}$ is the space–time flux vector, $\vec{n}$ is the outward unit normal vector and $ds$ is the area of a surface element on $S(V)$. Writing the part on the left side of Eq. (22) in an extended form, we have

$$\oint\limits_{S(V)} \vec{H} \cdot d\vec{s} = \iint\limits_{A'C'E'G'} Qdrdz - \iint\limits_{ACEG} Qdrdz + \iint\limits_{C'CEE'} Edzdt - \iint\limits_{A'AGG'} Edzdt + \iint\limits_{G'GEE'} Fdrdt - \iint\limits_{A'ACC'} Fdrdt, \tag{23}$$

where A′C′E′G′, ACEG, C′CEE′, A′AGG′, G′GEE′ and A′ACC′ are the surface elements of the CE boundary.

When integrating Eq. (22), we notice that CE(P′) is related to SE(P′) as well as SE (A), SE (C), SE (E) and SE (G). The values of physical variables on point P′ are calculated from mesh points A, C, E and G. The integration over the surface element C′CEE′ which is related to SE (C) and SE (E), for example, can be separated into two parts:

$$\iint\limits_{C'CEE'} Edzdt = \iint\limits_{C'CDD'} Edzdt + \iint\limits_{D'DEE'} Edzdt. \tag{24}$$

Here an approximation, that the value at the center point of a surface is considered as the average value of the surface, is made. Then we have

$$\iint\limits_{C'CEE'} Edzdt = \frac{1}{4}\Delta z \Delta t \cdot E\left(0, \frac{\Delta z}{4}, \frac{\Delta t}{4}\right)_C + \frac{1}{4}\Delta z \Delta t \cdot E\left(0, -\frac{\Delta z}{4}, \frac{\Delta t}{4}\right)_E. \tag{25}$$

The integrations over all other surface elements are solved in the same way. The time and the space integrations are treated by the same method. At last, we obtain the following expression from Eq. (22):

$$(Q_m)_{P'} - \frac{\Delta t}{4}(S_m)_{P'} = \frac{1}{4}\left(\overline{Q} + \frac{\Delta t}{\Delta r}\overline{E} + \frac{\Delta t}{\Delta z}\overline{F} + \frac{\Delta t}{4}\overline{S}\right), \tag{26}$$

where

$$\overline{Q} = Q_m\left(\frac{\Delta r}{4}, \frac{\Delta z}{4}, 0\right)_A + Q_m\left(-\frac{\Delta r}{4}, \frac{\Delta z}{4}, 0\right)_C + Q_m\left(-\frac{\Delta r}{4}, -\frac{\Delta z}{4}, 0\right)_E + Q_m\left(\frac{\Delta r}{4}, -\frac{\Delta z}{4}, 0\right)_G, \tag{27}$$

$$\overline{E} = E_m\left(0, \frac{\Delta z}{4}, \frac{\Delta t}{4}\right)_A - E_m\left(0, \frac{\Delta z}{4}, \frac{\Delta t}{4}\right)_C - E_m\left(0, -\frac{\Delta z}{4}, \frac{\Delta t}{4}\right)_E + E_m\left(0, -\frac{\Delta z}{4}, \frac{\Delta t}{4}\right)_G, \tag{28}$$

$$\overline{F} = F_m\left(\frac{\Delta r}{4}, 0, \frac{\Delta t}{4}\right)_A + F_m\left(-\frac{\Delta r}{4}, 0, \frac{\Delta t}{4}\right)_C - F_m\left(-\frac{\Delta r}{4}, 0, \frac{\Delta t}{4}\right)_E - F_m\left(\frac{\Delta r}{4}, 0, \frac{\Delta t}{4}\right)_G, \tag{29}$$

$$\overline{S} = (S_m)_A + (S_m)_C + (S_m)_E + (S_m)_G. \tag{30}$$

Using the continuous conditions at point A′, C′, E′ and G′, we have the derivatives of $Q_m$ with respect to r and z:

$$(Q_{mr})_{P'} = W\left[(Q_{mr})_{P'}^-, (Q_{mr})_{P'}^+, \chi\right], (Q_{mz})_{P'} = W\left[(Q_{mz})_{P'}^-, (Q_{mz})_{P'}^+, \chi\right], \tag{31}$$

where the weighted equation is $W[f_-, f_+, \chi] = \frac{|f_+|^\chi f_- + |f_-|^\chi f_+}{|f_+|^\chi + |f_-|^\chi}$, $\chi$ is an adjustable constant which usually equals 1 or 2,

$$(Q_{mr})_{P'}^- = -\frac{1}{\Delta r}\left[Q_m\left(0, 0, \frac{\Delta t}{2}\right)_A + Q_m\left(0, 0, \frac{\Delta t}{2}\right)_G - 2(Q_m)_{P'}\right], \tag{32}$$

$$(Q_{mr})_{P'}^+ = +\frac{1}{\Delta r}\left[Q_m\left(0, 0, \frac{\Delta t}{2}\right)_C + Q_m\left(0, 0, \frac{\Delta t}{2}\right)_E - 2(Q_m)_{P'}\right], \tag{33}$$

$$(Q_{mz})_{P'}^- = -\frac{1}{\Delta z}\left[Q_m\left(0, 0, \frac{\Delta t}{2}\right)_A + Q_m\left(0, 0, \frac{\Delta t}{2}\right)_C - 2(Q_m)_{P'}\right], \tag{34}$$

$$(Q_{mz})_{P'}^+ = +\frac{1}{\Delta z}\left[Q_m\left(0, 0, \frac{\Delta t}{2}\right)_E + Q_m\left(0, 0, \frac{\Delta t}{2}\right)_G - 2(Q_m)_{P'}\right]. \tag{35}$$

It should be noted that $(Q_m)_{P'}$ cannot be obtained explicitly from Eq. (26) due to the source term $(S_m)_{P'}$. As $(S_m)_{P'}$ is a function of $(Q_m)_{P'}$, a local Newton iterative procedure is usually needed to determine $(Q_m)_{P'}$. In the present work, in order to save computation time, we replace $(S_m)_{P'}$ with its linear prediction of current time in Eq. (26), i.e.,

$$(Q_m)_{P'} = \frac{1}{4}\overline{Q} + \frac{\Delta t}{4\Delta r}\overline{E} + \frac{\Delta t}{4\Delta z}\overline{F} + \frac{\Delta t}{2}\widetilde{S}, \tag{36}$$

$$\widetilde{S} = \overline{S} + \frac{\Delta t}{2}\overline{S}_t, \tag{37}$$

where $\overline{S}_t$ is the time derivative of $\overline{S}$. In our numerical tests, the results of linear approximation agree with those of Newton iteration, which indicates that the linear approximation of $(S_m)_{P'}$ is reasonable. More detailed description of the improved CE/SE scheme is available in Ref. [35].

## 4. Interface capturing algorithm

The hybrid particle LSM [20] is used to describe the material interfaces including the plane where spallation takes place. We adopt separate level set functions to describe interfaces of multiple materials as illustrated in Fig. 3. Only one material can possess a given computational grid point at any moment. The governing equations for each material are solved respectively in the region $\varphi(\vec{x}, t) < 0$ of each level set function, and then the level set functions are reevaluated according to the material velocity fields.

### 4.1. Level set method

The fundamental idea of the LSM is to represent an interface $\Gamma$ which bounds an open region $\Omega$ as the zero level set of a higher dimensional scalar function $\varphi(\vec{x}, t)$. The level set function in the present paper is defined as

$$\begin{aligned} \varphi(\vec{x}, t) &< 0 \quad \vec{x} \in \Omega_1, \\ \varphi(\vec{x}, t) &= 0 \quad \vec{x} \in \Gamma, \\ \varphi(\vec{x}, t) &> 0 \quad \vec{x} \in \Gamma_2, \end{aligned} \tag{38}$$

where $\Omega_1$ is the inside part of a material, $\Gamma$ is the interface and $\Omega_2$ is out of the material boundary. The motion of the interface is determined by a velocity field $\vec{U}$, which may depend on position, time or geometry of the interface. The evolution of the level set function is given by a convection equation:

$$\frac{d\varphi}{dt} = \frac{\partial \varphi}{\partial t} + \vec{U} \cdot \nabla \varphi = 0, \tag{39}$$

which only needs to be solved locally near the interface [44,45]. It is convenient to treat $\varphi$ as a function of the signed distance to the interface. Geometrical quantities including the unit normal, pointing from inside to outside of the region, and the curvature can be calculated from the level set function by

$$\vec{n} = \frac{\nabla \varphi}{|\nabla \varphi|}, \quad \kappa = \nabla \cdot \frac{\nabla \varphi}{|\nabla \varphi|}. \tag{40}$$

As noted in Ref. [46], however, the level set function will cease to be a signed distance function after several computational steps especially for flows undergoing extreme topological changes. As a result, reinitialization algorithms are needed to maintain the signed distance property by solving to steady state the equation

$$\begin{cases} \Phi_\tau = \text{sign}(\varphi)(1 - |\nabla \Phi|), \\ \Phi(\vec{x}, 0) = \varphi(\vec{x}, t), \end{cases} \tag{41}$$

where $\tau$ is fictitious time, $\text{sign}(\varphi)$ is a signum function numerically approximated as

$$\text{sign}(\varphi) = \frac{\varphi}{\sqrt{\varphi^2 + \varepsilon^2}}, \tag{42}$$

where $\varepsilon$ is a parameter related to the mesh size (e.g., $\varepsilon = \min(\Delta r, \Delta z)$). Also, Eq. (41) only needs to be solved locally near the interface. A fifth-order WENO scheme and a third-order Runge–Kutta scheme are adopted to calculate the spatial and the temporal derivatives, respectively, in Eqs. (39) and (41).

### 4.2. Hybrid particle level set method

Due to excessive regularization caused by dissipation of the numerical scheme and the reinitialization procedure, sharp corners are rounded off and objects may lose mass during large deformations. In order to rectify the error, Enright et al. [20] introduced Lagrangian massless marker particles in combination with the LSM which is implemented in the Eulerian framework. The particles are used to both track characteristic information and reconstruct the interface in regions where the LSM has failed to accurately preserve mass.
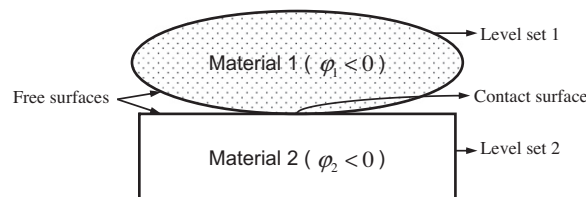


Fig. 3. Illustration of material surfaces and level set functions. Separate level set functions are used to describe surfaces of multiple materials.

Two sets of marker particles, the positive particles and the negative particles, are defined. The positive particles lie in the region where $\varphi > 0$ while the negative particles are in the $\varphi < 0$ region. The particles are advected with the evolution equation

$$\frac{d\vec{x}_p}{dt} = \vec{U}(\vec{x}_p),$$ (43)

where $\vec{x}_p$ is the position of the particle and $\vec{U}(\vec{x}_p)$ is its velocity. The particle velocities are interpolated from velocities of the surrounding grids which contain the center of the particle. A third-order accurate Runge–Kutta method is used to evolve the particle positions forward in time. The radius of each particle is in the range of $(a_{min}, a_{max})$ where

$$a_{min} = 0.1 \, \min(\Delta r, \Delta z), \quad a_{max} = 0.5 \, \min(\Delta r, \Delta z),$$ (44)

according to Ref. [20]. This allows multiscale particle resolution of the interface.

First of all, particles of both signs are randomly seeded in the elements that are within the distance of $3\max(\Delta r, \Delta z)$ from the interface. For the purpose of interface reconstruction, the particles are allowed to overlap as illustrated in Fig. 4, which enables us to reconstruct the interface exactly as the number of particles approaches infinity. Four particles per spatial dimension (i.e., 4 in 1D, 16 in 2D and 64 in 3D) are distributed in each cell. Afterward, particles are attracted to the correct side of the interface (positive particles to the $\varphi > 0$ side and negative particles to the $\varphi < 0$ side) into a band between a distance of $b_{min}$ and $b_{max}$ of the interface, where

$$b_{min} = a_{min}, \quad b_{max} = 3\max(\Delta r, \Delta z).$$ (45)

The attraction equation is

$$\vec{x}_{new} = \vec{x}_p + \lambda\left(\varphi_{goal} - \varphi(\vec{x}_p)\right)\vec{n}(\vec{x}_p),$$ (46)

where $\varphi_{goal}$ is a random value in $(b_{min}, b_{max})$ for a positive particle or in $(-b_{max}, -b_{min})$ for a negative particle so that the distribution of particles in the direction normal to the interface is random. The parameter $\lambda$ is set to 1 at the beginning and is successively halved until Eq. (46) places the particle within the expected domain. If the particle does not lie in the desired region after a certain number (e.g., we use 16) of iterations, it is deleted. Finally, each particle radius is set as

$$a_p = \begin{cases} a_{max} & \text{if } s_p\varphi(\vec{x}_p) > a_{max}, \\ s_p\varphi(\vec{x}_p) & \text{if } a_{min} \leqslant s_p\varphi(\vec{x}_p) \leqslant a_{max}, \\ a_{min} & \text{if } s_p\varphi(\vec{x}_p) < a_{min}, \end{cases}$$ (47)

where $s_p$ is the sign of the particle (+1 for positive particles and $-1$ for negative particles).

After each time step, the marker particles are employed to correct possible errors in the level set function due to the non-physical deletion of merging characteristics. The level set function of each particle is determined by local interpolation of the surrounding grid points. A particle is defined as escaped only when it crosses the interface by more than its radius, as is shown in Fig. 4. Each particle can be represented as a locally defined level set function:

$$\varphi_p(\vec{x}) = s_p(|\vec{x} - \vec{x}_p| - a_p),$$ (48)

where $a_p$ is the radius of the particle, $\vec{x}_p$ is the position of the particle center. The zero level set of $\varphi_p$ corresponds to the boundary of the particle.

We use the escaped positive particles $E^+$ to rebuild the $\varphi > 0$ region and the escaped negative particles $E^-$ to rebuild the $\varphi < 0$ region. Each $\varphi_p$ is compared to the local value of $\varphi$ and the maximum of these two values is taken as $\varphi^+$, we initialize $\varphi^+$ with $\varphi$ and then calculate

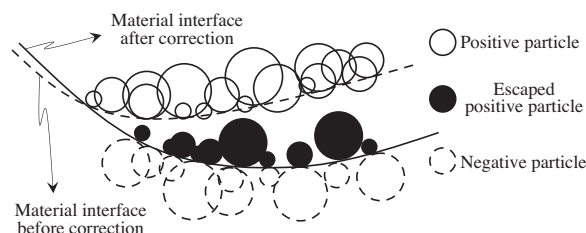$$\varphi^+ = \max_{\forall p \in E^+}(\varphi_p, \varphi^+).$$ (49)



**Fig. 4.** Illustration of error correction of the level set function by using escaped positive particles.

Similarly, to calculate a reduced error representation of the $\varphi < 0$ region, we initialize $\varphi^-$ with $\varphi$ and then calculate

$$\varphi^- = \min_{\forall p \in E^-}(\varphi_p, \varphi^-). \tag{50}$$

We merge $\varphi^+$ and $\varphi^-$ back into a single level set by setting

$$\varphi = \begin{cases} \varphi^+ & \text{if } |\varphi^+| \leqslant |\varphi^-|, \\ \varphi^- & \text{if } |\varphi^+| > |\varphi^-|, \end{cases} \tag{51}$$

which is least in magnitude at each grid point.

Since the reinitialization may cause the zero level set to move, we use the marker particles to correct the errors in the level set function as well. After the radii of the particles are adjusted, the particle reseeding process is performed.

In flows with interface stretching and tearing, regions which lack sufficient marker particles will arise. To accurately capture the interface, a so-called reseeding procedure must be performed periodically to readapt the particle distribution to the deformed interface. Reseeding is carried out by first identifying all the nonescaped particles in each cell. The local value of the level set function is used to determine whether a given cell is near the interface. If a cell is not near the interface, all the nonescaped particles are deleted. If a cell near the interface currently has fewer particles than the previously defined maximum, particles are added to the cell and attracted to the interface. In addition, escaped particles should not be deleted.

### 4.3. Particle level set representation of a crack

In many applications, a crack is modeled as an open curve, as illustrated in Fig. 5(a), in the two-dimensional framework [23,24,47,48]. It is effective to model a crack as a curve when the crack keeps narrow since only the propagation of the crack needs to be performed. In the spall fracture, however, the scab moves away from the target plate after the crack appears. As a result, the crack opens wide with the motion of the scab. If the crack is still modeled as an open curve, the scab will never separate from the target plate, which is in contradiction with the experimental observation. Furthermore, an initial crack needs to be constructed in the material according to Stolarska's method [23]. But the target plate, in a spall experiment, does not have a macroscopic crack before the spall fracture appears. It is unreasonable to put a crack in the target before simulation. Thus a different representation of a crack by level set is needed.

In the simulations, we monitor the spatio-temporal evolution of the void volume fraction (VVF) which is the porosity $\phi$ in the VG model. Eftis has shown analytically that the yield function becomes zero as the VVF reaches a critical value [49], at which the material loses its strength and the microelement of the material experiences separation as the rate of inelastic deformation increases dramatically. The critical value of the VVF for copper has been analytically calculated to be 0.3 [49]. Hence, the spallation is assumed to take place when the VVF of a computational cell reaches the critical value in our simulations.

In order to describe the formation and the propagation of a crack, we choose to delete the element whose VVF reaches the critical value. The element here refers to the projection of the SE on the $roz$ plane. The deletion of the element is implemented by a logical operation on the two level set functions which represent the area of the target plate and the area of the failed element respectively. After the logical operation, the area of the failed elements turns to $\varphi > 0$. Noticing that the area $\varphi > 0$ is not calculated in our simulation, we treat the material in this area as void whose density is set to zero. Then the interface capturing strategy described above is used to solve the regions where the spall happens. Notice that the strategy for capturing interfaces where spall happens has no difference from that of the ordinary interfaces. For example, when the VVF of point P in Fig. 5(c) reaches the critical value, the element which contains point P will be subtracted from the target by the logical operation. A crack is formed after all the failed elements are deleted, as is shown in Fig. 5(b). The crack formed here is not a curve but a two-dimensional narrow region where $\varphi > 0$. The crack can be in any shape according to the specific problem.
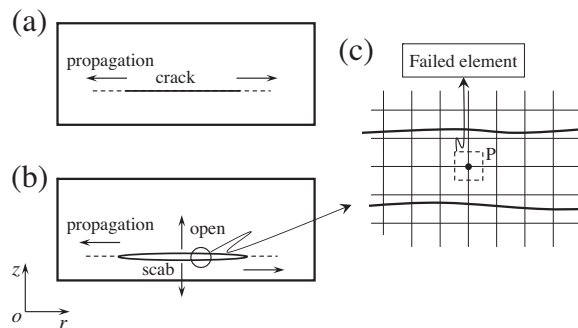


**Fig. 5.** Comparison between the traditional representation of a crack by level set and the representation proposed in the present paper. (a) Traditional representation of a crack. (b) Representation of a crack in the present paper. (c) Partial enlarged view of (b).

Additional interfaces are created between the failed elements areas and the areas of the non-failed elements due to the crack. The particles are seeded on both sides of an interface and attracted to the correct sides of the interface. Then the reseeding process is implemented each time step. This procedure is the same as particles seeding and reseeding on the initial surfaces.

## 5. Boundary conditions

The boundary points of a material are, by definition, the mesh points that are out of the region of the material but are needed during the process of the computation. In the axisymmetric case, the CE/SE scheme needs only one boundary point at the boundary of $r$ or $z$ direction. All boundary points can be classified into the contact boundary points and the free boundary points. The former describes the interaction between two material blocks, and the latter describes the movement of the free surface in vacuum. The mesh point is identified as the contact boundary point if it is a boundary point of a certain material and locates in the other material, or the free boundary point if it is a boundary point of one material and does not locate in any other materials.

The values of the boundary points of a material are obtained from that of the points inside the material or the points of the material in vicinity, according to the physical boundary conditions such as the free boundary conditions or the contact boundary conditions. When the shock reaches the interface, this boundary treatment leads to a local reduction in order of accuracy at the grid points by the interfaces. However, the high-order accuracy is still maintained in the bulk of the computational domain. Similar applications to the multimaterial interfaces can be found in [19,35,50] for the treatment of shock and contact discontinuities.

### 5.1. Free boundary conditions

The physical conditions on a free surface are that the normal stress components are zero. For the axisymmetric case, we introduce local coordinates associated with the interface normal and tangent vectors. In the local coordinates the stress tensor can be rotated by

$$\boldsymbol{\sigma}' = A^{\mathrm{T}} \boldsymbol{\sigma} A, \tag{52}$$

where $\boldsymbol{\sigma}' = \begin{bmatrix} \sigma_{nn} & \sigma_{n\tau} \\ \sigma_{\tau n} & \sigma_{\tau\tau} \end{bmatrix}$, $A = \begin{bmatrix} n_r & -n_z \\ n_z & n_r \end{bmatrix}$, $n_r$ and $n_z$ are the components of the unit normal vector in $r$ and $z$ directions, and

$\boldsymbol{\sigma} = \begin{bmatrix} \sigma_{rr} & \sigma_{rz} \\ \sigma_{zr} & \sigma_{zz} \end{bmatrix}$. The normal stress components $\sigma_{nn}$ and $\sigma_{nt}$ are zero on the free surface while the tangential stress component $\sigma_{\tau\tau}$ is not.

Suppose that point $P$, as is shown in Fig. 6(a), is a free boundary point. The stress components of point $I$ which is at the mirror position of point $P$ in the local coordinates can be calculated by

$$
\begin{aligned}
\sigma_{nn,I} &= n_{r,P}^2 s_{rr,I} + n_{z,P}^2 s_{zz,I} + 2 n_{r,P} n_{z,P} s_{rz,I} - p_I, \\
\sigma_{n\tau,I} &= \left( n_{r,P}^2 - n_{z,P}^2 \right) s_{rz,I} + n_{r,P} n_{z,P} (s_{zz,I} - s_{rr,I}), \\
\sigma_{\tau\tau,I} &= n_{r,P}^2 s_{zz,I} + n_{z,P}^2 s_{rr,I} - 2 n_{r,P} n_{z,P} s_{rz,I} - p_I,
\end{aligned}
\tag{53}
$$

where subscript $I$ denotes values at point I, $n_{r,P}$ and $n_{z,P}$ are the components of the unit normal vector in $r$ and $z$ directions at point $P$, which can be computed from the level set function. Considering the fact that the normal stress components are zero on the surface and point I is the mirror point of point $P$, the following relations can be obtained:

$$\sigma_{nn,P} = -\sigma_{nn,I}, \quad \sigma_{n\tau,P} = -\sigma_{n\tau,I}, \quad \sigma_{\tau\tau,P} = \sigma_{\tau\tau,I}. \tag{54}$$
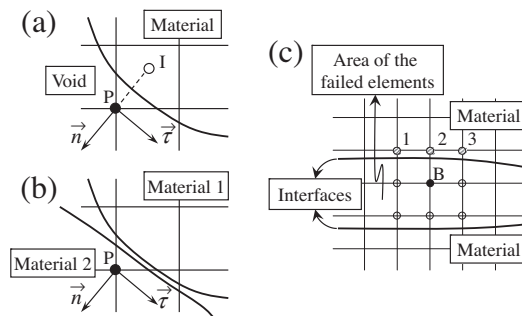


**Fig. 6.** Illustration of the boundary conditions. (a) Free boundary conditions. (b) Contact boundary conditions. (c) Extrapolation process for boundary points in the area of the failed elements.

The stress components can be easily converted from the local coordinates to the global Cartesian coordinates by Eq. (52). All other variables such as the density, the velocity and the internal energy are extrapolated linearly from the inside of the material to point $P$.

### 5.2. Contact boundary conditions

Here we consider the sliding interface. The physical conditions imposed on the sliding interface are that the normal velocity and the normal stress components crossing the interface between the two materials are continuous, whereas the tangential velocity and the tangential stress components may remain discontinuous. Suppose point $P$, as illustrated in Fig. 6(b), is a contact boundary point of material 1. Then point $P$ is in material 2, according to the definition of the contact boundary point.

In the local coordinates the velocity vector is

$$\mathbf{v}' = A^T \mathbf{v}, \tag{55}$$

where $\mathbf{v}' = \begin{bmatrix} v_n \\ v_\tau \end{bmatrix}$ and $\mathbf{v} = \begin{bmatrix} u \\ v \end{bmatrix}$.

Given Eq. (55) and the velocity conditions on the sliding interface, the velocity at point $P$ in the local coordinates can be written as

$$
\begin{aligned}
v_n &= u_{P,2} n_r + v_{P,2} n_z, \\
v_\tau &= -u_{P,1} n_z + v_{P,1} n_r,
\end{aligned}
\tag{56}
$$

where subscript 1 denotes the linearly extrapolated values from material 1, and subscript 2 denotes the actual velocity at point $P$ in material 2. Using Eq. (55), we can obtain the velocity components at point $P$ in the global Cartesian coordinates by

$$u_P = v_n n_r - v_\tau n_z, \quad v_P = v_n n_z + v_\tau n_r. \tag{57}$$

With the stress conditions on the sliding interface and Eq. (52), the components of the stress tensor are calculated from

$$
\begin{aligned}
\sigma_{\tau\tau} &= n_{r,P}^2 s_{zz,1} + n_{z,P}^2 s_{rr,1} - 2 n_{r,P} n_{z,P} s_{rz,1} - p_1, \\
\sigma_{nn} &= n_{r,P}^2 s_{rr,2} + n_{z,P}^2 s_{zz,2} + 2 n_{r,P} n_{z,P} s_{rz,2} - p_2, \\
\sigma_{n\tau} &= n_{r,P} n_{z,P} (s_{zz,2} - s_{rr,2}) + \left( n_{r,P}^2 - n_{z,P}^2 \right) s_{rz,2}.
\end{aligned}
\tag{58}
$$

It is easy to convert the stress components from the local coordinates to the global Cartesian coordinates by Eq. (52). As the case of the free surface boundary conditions, all other variables such as the density, the velocity and the internal energy are extrapolated linearly from material 1 to point $P$.

### 5.3. Boundary conditions for failed region

In the domain of the deleted elements, we find that the level set function is no longer a signed distance function. The unit normal of any free boundary point can not be calculated from $\varphi$. As a result, the free boundary conditions described above are not available to the boundary points in the area of the failed elements. In order to extrapolate values from the interior of a material to the boundary point $B$ which is surrounded by the eight grid points, as illustrated in Fig. 6(c), the distance-weighted interpolation is performed from the three surrounding grid points (Point 1, 2 and 3) that lie inside the undamaged material.

## 6. Applications

The geometrical scketch of a plate-impact experiment [38] for the research of spall fracture, consisting essentially of a thin flyer plate that acts as a high-speed projectile and a target plate, is illustrated in Fig. 7. The flyer plate has a high velocity and the target plate is at rest before impact. Owing to the fact that the plates used in the experiment are usually cylindrical,
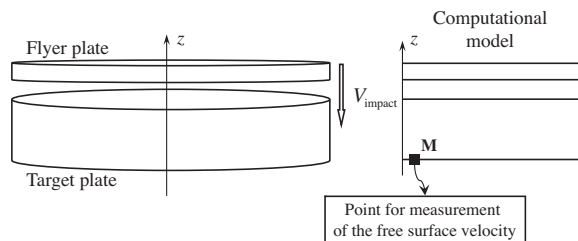


**Fig. 7.** Schematic of numerical simulation for the plate-impact experiment. Point M on the backside of the target indicates the grid point where the free-surface-velocity history is monitored.

the situation considered here is axisymmetric in nature. Since the diameters of both the flyer and the target are much greater than their thicknesses, most part inside both plates is under uniaxial strain conditions and only the material near the lateral boundary is influenced by the edge effects. Point $M$ in Fig. 7, which is at the rear surface of the target plate and close to the symmetric axis, is selected for capturing the velocity history of the particle at the free surface.

The predictions of the proposed computational methodology are compared to the experiments [38], including spall thicknesses of scabs and particle velocity profiles at the target free surface. Details of the experiments that are simulated in the present work are listed in Table 1. The material parameters of the target plates used in the simulations for various kinds of models are listed in Table 2. The constitutive model and the EOS for the flyer plate are the Johnson–Cook model [41,42] and the MG EOS, respectively.

### 6.1. Stainless steel plates impacted by aluminum plates at two different speeds

The mesh dependency is investigated for the case of a stainless steel plate collided by an aluminum plate at $V = 700$ m/s. The location and the breadth of the damaged zone are described in Fig. 8 at $t = 3.5$ μs when the spall fracture is completed. The flyer thickness is $h_f = 2$ mm, and the target thickness is $h_t = 10$ mm. All the meshes adopted here are square. Three different mesh dimensions are tested: from 0.133 mm each side for the coarse mesh to 0.067 mm for the dense mesh. An element is deleted when its porosity reaches the critical value $VVF_c = 0.3$. The zone of the failed elements, as is shown in Fig. 8, is 0.3 mm in breadth. No mesh dependency is observed when the mesh size is below 0.1 mm. Thus the grid size of 0.1 mm is adopted in the following calculations. The numerical results are also mesh independent with the same grid size for the other impact velocities in the present work. The same trend is observed for the velocity profiles at the free surface.

Simulations of stainless steel target plates collided by aluminum flyer plates at two different speeds which are $V = 445$ m/s and $V = 700$ m/s have been performed. We use Point M, as illustrated in Fig. 7, to capture the history of particle velocities at the free surface. The numerical results are compared to the experimental data, as is shown in Fig. 9. According to the experimental plot [38], time $t = 0$ corresponds to the moment when particles at the free surface start to move. The so-called "velocity pullback" $\Delta v$ and the period of the velocity oscillation $T_p$ are denoted in the figure. It is observed that the profiles of the numerical results and the experimental data agree with each other well, especially for the velocity pullback. The velocity pullback by simulation is 107 m/s and the experimental value is 101 m/s at speed 445 m/s. The relative error is 6%. For speed 700 m/s, the velocity pullback by simulation is 106 m/s and the experimental value is 109 m/s. The relative error is 3%. The peak value of the velocity profiles is higher when the target plate is collided by a higher velocity. The period

**Table 1**
Detailed information of experiments to be calculated in the following work.

| Experiment number | Flyer plate | | | | Target plate | | |
|---|---|---|---|---|---|---|---|
| | Material | Thickness (mm) | Diameter (mm) | Velocity (m/s) | Material | Thickness (mm) | Diameter (mm) |
| B33 | Aluminum | 2 | 120 | 700 ± 30 | Stainless steel | 10 | 120 |
| B34 | Aluminum | 2 | 120 | 445 ± 15 | Stainless steel | 10 | 120 |
| B61 | Aluminum | 2 | 120 | 450 ± 20 | Copper | 15 | 120 |

**Table 2**
Material parameters of the target plates for the EOS, the constitutive equation and the VG model.

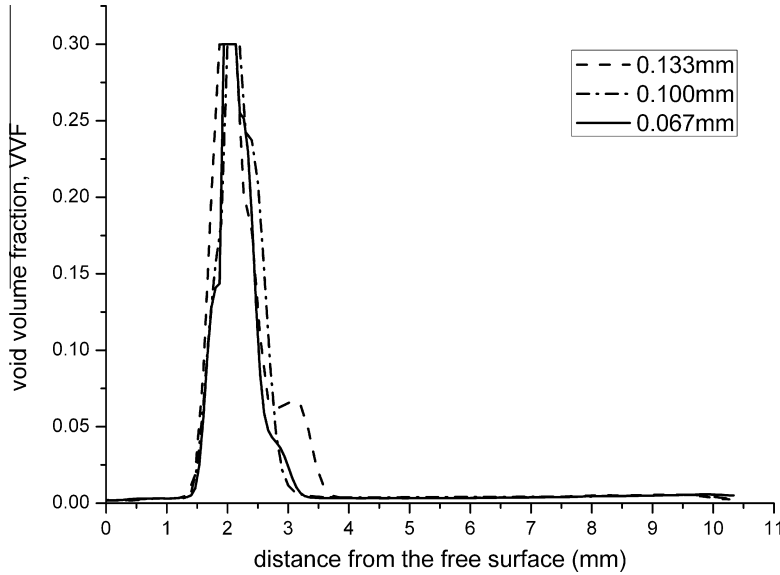| | Parameters | Stainless steel | Copper |
|---|---|---|---|
| | $\rho_0$ (kg/m$^3$) | 7900 | 8930 |
| | $C$ (J/kg · K) | 423 | 395 |
| | $T_m$ (K) | 2380 | 1356 |
| The MG EOS | $\gamma_0$ | 1.93 | 1.98 |
| | $s$ | 1.49 | 1.33 |
| | $C_0$ (m/s) | 4650 | 3960 |
| The SG model | $Y_0$ (Pa) | $3.0 \times 10^8$ | $9.0 \times 10^7$ |
| | $Y_{max}$ (Pa) | $2.5 \times 10^9$ | $6.4 \times 10^8$ |
| | $G_0$ (Pa) | $81.4 \times 10^9$ | $43.3 \times 10^9$ |
| | $G'_p$ | 1.74 | 1.35 |
| | $G'_T$ (Pa) | $-3.504 \times 10^7$ | $-1.798 \times 10^7$ |
| | $Y'_p$ | 0.007684 | 0.003396 |
| | $\beta$ | 43 | 36 |
| | $n$ | 0.35 | 0.45 |
| The VG model | $\alpha_0$ | 1.0006 | 1.0003 |
| | $\eta$ (Pa · s) | 1.0 | 1.0 |
| | $a_s$ (Pa) | $0.3911 \times 10^9$ | $0.17 \times 10^9$ |

**Fig. 8.** Effect of mesh size on the VVF distribution inside the target plate, for impact velocity $V = 700$ m/s, at the instant when $t = 3.5$ μs.
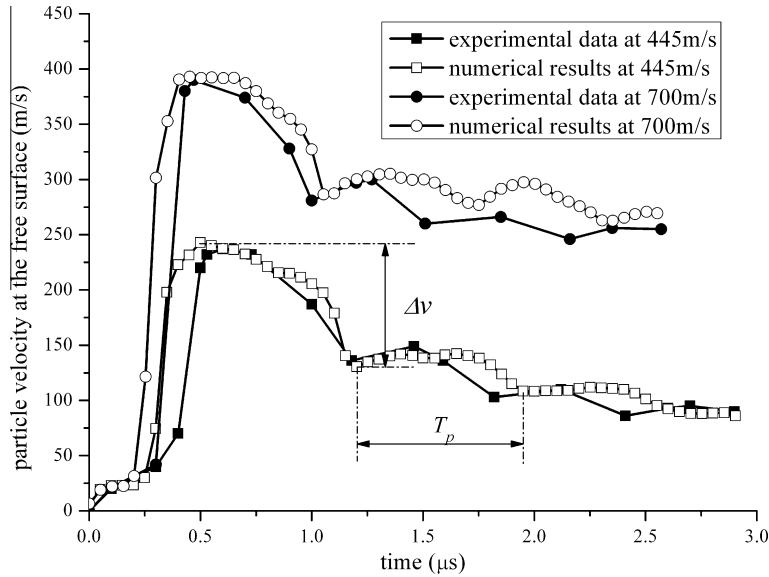


**Fig. 9.** Comparison of free surface particle velocity profiles between results of simulations and experimental plots at different impact velocities: $V$ = 445 and 700 m/s.

of velocity oscillation can be measured from the thickness of the scab. The velocity pullback $\Delta v$ is a measure of incipient fracture strength of the material. The results of our simulation, as indicated in Fig. 9, show that increase of impact velocity does not influence the magnitude of the velocity pullback, which is also observed by many experiments of different materials [38,51]. The spall strength ($\sigma_{sp}$) and the thickness ($h$) of the scab are related to the velocity pullback and the speed oscillation period by the following expressions [2], respectively:

$$\sigma_{sp} = \frac{1}{2}\rho_0 C_0 \Delta v, \tag{59}$$

$$h = \frac{1}{2}C_0 T_p, \tag{60}$$

where $\rho_0$ and $C_0$ are the density and the bulk sound speed at zero pressure. The numerical results for some key physical parameters, compared to the experimental data, are listed in Table 3. The spall strengths of the two impact speeds both

**Table 3**
Comparison of numerical results and experimental data.

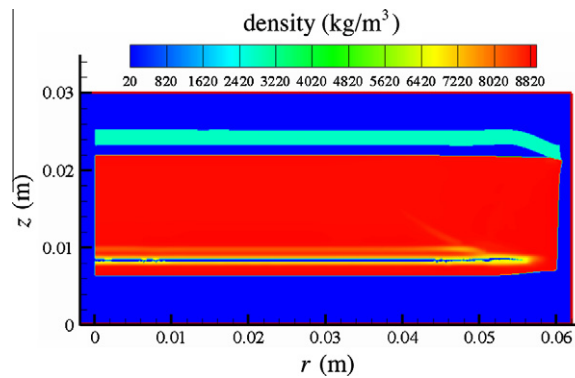|  | Spall strength | | Thickness of scab | |
| --- | --- | --- | --- | --- |
| Impact velocity (m/s) | 445 | 700 | 445 | 700 |
| Experiments | 1.93 ± 0.13 GPa | 1.93 ± 0.09 GPa | 1.78 mm (±10%) | 1.61 mm (±10%) |
| Simulations | 2.06 GPa | 1.96 GPa | 1.74 mm | 1.62 mm |



**Fig. 10.** Contour plot of the material density at time $t = 7.0$ μs when the spall fracture is completed. The impact velocity is 450 m/s. Line $r = 0$ is the axis of symmetry.

locate within the range of the experiments. A decrease of the thickness of the scab can be observed from the simulations with increase in flyer velocity, which is in accord with the experimental phenomenon.

### 6.2. A copper plate impacted by an aluminum plate at a speed of 450 m/s

The simulation of a 15 mm-thick copper plate impacted by a 2 mm-thick aluminum plate at a speed of 450 m/s has been performed. Fig. 10 presents the contour plot of material density at time $t = 7.0$ μs when the spall fracture is accomplished. The superposition of the rarefaction waves has produced a large tensile mean stress causing a localized damage. It can be observed that the density near the spall plane is lower than the normal density of copper, which indicates that the microvoiding process does exist before spallation. In the numerical simulation, the incident shock wave is attenuated not only by the axial unloading waves but also by the release waves from the lateral. Due to this extra attenuation, the scab does not separate from the target plate, as is shown in Fig. 10, being held back by the less-fractured periphery. Another phenomenon which is worth noticing is that there is a second plane of lower density inside the target plate. When the first scab is produced, the tensile wave has not been released thoroughly and continues to propagate into the target plate. As a result, another region of lower density appears. We believe that a second scab can be simulated if the tensile wave is strong enough and lasts for plenty of time. The scab by simulation is about 1.6 mm thick while the experimental thickness of the scab is 1.24 mm (±10%). Maybe the material parameters used in the simulation are not the best-fit values for the materials used in the experiments. Or a more advanced spall model may help to improve the numerical results. Although beyond the range of the experimental data, the numerical result is close to satisfaction.

Fig. 11 presents the distribution of void volume fraction (VVF) in the target at three different moments during the process of impact. Time $t = 0$ corresponds to the instant when the flyer plate contacts the target plate. Fig. 11(a) shows the initiation of the porosity in the target. Owing to the interaction of rarefaction waves coming from the bottom boundary and the side boundary, the VVF near the right side bottom of the target has the highest value. We may deduce that microvoids are initiated earlier in the target near the lateral boundary. In Fig. 11(b), the failed area which looks like a small hole is displayed clearly. A larger porosity is cumulated near the lateral boundary first. Some elements have been deleted and a crack is initiated as the VVF reaches the critical value 0.3. At the end of the test, as illustrated in Fig. 11(c), the crack has finished propagation in the whole plane of spallation and the spall fracture is completed. A scab of about 1.6 mm thick is pointed out in the picture. The region which displays the other peak value of the VVF in Fig. 11 is relevant to the second plane of lower density discussed above. A second scab is not formed since the VVF cannot reach the critical value.

The comparison between the numerical results and the experimental data of particle velocity at the free surface is shown in Fig. 12. The particles at the free surface are stationary initially. According to the experimental plot [38], time $t = 0$ is relevant to the moment when particles on the back side of the target start to move. It can be observed from Fig. 12 that the velocity history obtained by computation essentially coincides with the experimental profile. Particle velocity at the free surface keeps rising with the propagation of compressive waves. The velocity reaches a peak value and starts to decrease when
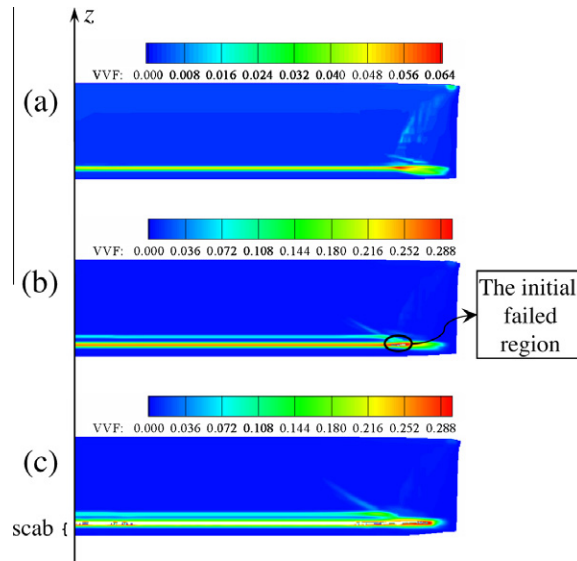
**Fig. 11.** The evolution of the void volume fraction (VVF) inside the target during the impact process. (a) $t = 4.2$ μs; (b) $t = 5.1$ μs; (c) $t = 7.0$ μs.
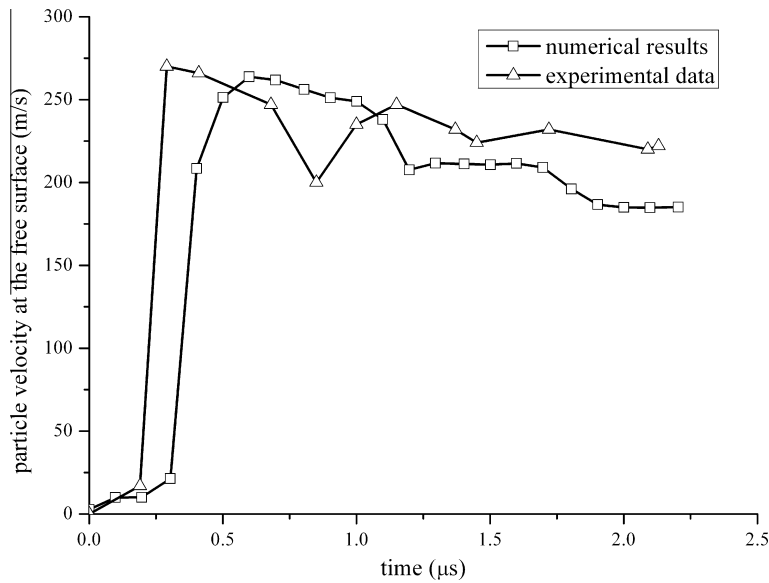


**Fig. 12.** Comparison of the computational and the experimental free surface particle velocity profiles. The impact velocity is 450 m/s.

the tensile stress caused by the reflection of compressive waves inside the target is observed. When the peak value of the tensile stress reaches the spall threshold, damage begins to accumulate. The tensile stress in the zone where damage accumulates decreases as the microvoiding process develops. Consequently, a compressive disturbance appears on the free surface velocity profile, which is considered as a signal when the spall happens. Henceforth wave reverberation continues between the free surface and the spall plane on the scab. Although the velocity pullback by simulation is on the same magnitude with the result from the experiment, it is obviously delayed. Maybe the zero point of the $t$-axis should be set to the instant when the flyer impacts the target since the minimum velocities which can be monitored by the experimental device and the computational simulation may be different.

## 7. Conclusions

The present paper has proposed an innovative computational methodology to simulate the spall fracture caused by high-velocity impact. The improved CE/SE scheme is applied to solve the high-velocity impact problems containing elastic–plastic

flows, high strain rates and spall fractures. The SG constitutive model and the MG EOS are used to describe the target materials. The VG model is introduced to monitor the VVF of each element. The hybrid particle LSM is adopted to capture the material interfaces and display the formation and propagation of a crack. The free surface boundary conditions and the contact boundary conditions are applied at the interfaces.

Numerical simulations for the spall fracture due to plate impact are carried out by the proposed technique. Several physical phenomena of the plate-impact spall, as were observed in the experiments, are exhibited in the numerical simulations: (a) the velocity pullback is displayed on velocity profiles of particles at the free surface; (b) the thickness of the scab decreases with increase in impact velocity; (c) the microvoiding process is clearly shown on the contour plots of the VVF at three different moments; (d) the edge effects are numerically reproduced, including the position of the crack initiation and the scab being held back at the periphery of the target. The simulations of stainless steel plates collided by aluminum plates show excellent agreement with the experimental data. The relative error of the velocity pullback is no more than 6%. The spall strength and the scab thickness by simulation both locate within the range of the experimental data. Qualitative agreement with the experiments is shown for the simulations of copper plate impacted by aluminum plate. In conclusion, the computational prediction is reliable.

Since the level set function is no longer a signed distance function in the domain of the deleted elements, a different boundary condition method is adopted in our simulation. The resolution of the method used here is lower. A boundary condition with higher resolution for the free surfaces at the spall plane should be helpful to the simulation. In addition, the spall model used in the present paper only considers the void growth process while the spall process consists of nucleation, growth and coalescence. A more advanced spall model will help to improve the simulation results.

In future work, several extensions of the methodology presented in this paper will be developed. The simulation of a more complicated spall fracture which occurs in the plate impacted by a spherical projectile is in process. In addition, extension to three-dimensions is relatively straightforward under this framework.

## Acknowledgements

## References

[1] D.R. Curran, L. Seaman, D.A. Shockey, Dynamic failure in solids, Phys. Today 30 (1) (1977) 46–55.
[2] T. Antoun, L. Seaman, D.R. Curran, et al, Spall Fracture, Springer, New York, 2003.
[3] D.R. Curran, L. Seaman, D.A. Shockey, Dynamic failure of solids, Phys. Rep. 147 (5–6) (1987) 253–388.
[4] M.A. Meyers, C.T. Aimone, Dynamic fracture (spalling) of metals, Prog. Mater. Sci. 28 (1) (1983) 1–96.
[5] J.N. Johnson, Dynamic fracture and spallation in ductile solids, J. Appl. Phys. 52 (4) (1981) 2812–2825.
[6] P. Perzyna, Internal state variable description of dynamic fracture of ductile solids, Int. J. Solids Struct. 22 (7) (1986) 797–818.
[7] J. Eftis, J.A. Nemes, Evolution equation for the void volume growth-rate in a viscoplastic-damage constitutive model, Int. J. Plasticity 7 (4) (1991) 275–293.
[8] J. Eftis, J.A. Nemes, P.W. Randles, Viscoplastic analysis of plate-impact spallation, Int. J. Plasticity 7 (1–2) (1991) 15–39.
[9] R. Cortes, The growth of microvoids under intense dynamic loading, Int. J. Solids Struct. 29 (11) (1992) 1339–1350.
[10] C. Czarnota, N. Jacques, S. Mercier, et al, Modelling of dynamic ductile fracture and application to the simulation of plate impact tests on tantalum, J. Mech. Phys. Solids 56 (4) (2008) 1624–1650.
[11] J. Eftis, C. Carrasco, R.A. Osegueda, A constitutive-microdamage model to simulate hypervelocity projectile-target impact, material damage and fracture, Int. J. Plasticity 19 (9) (2003) 1321–1354.
[12] V.R. Ikkurthi, S. Chaturvedi, Use of different damage models for simulating impact-driven spallation in metal plates, Int. J. Impact Eng. 30 (3) (2004) 275–301.
[13] D.J. Benson, computational methods in Lagrangian and Eulerian hydrocodes, Comput. Meth. Appl. Mech. Eng. 99 (2–3) (1992) 235–394.
[14] C.E. Anderson, An overview of the theory of hydrocodes, Int. J. Impact Eng. 5 (1987) 33–59.
[15] W.E. Johnson, C.E. Anderson, History and application of hydrocodes in hypervelocity impact, Int. J. Impact Eng. 5 (1987) 423–439.
[16] D.J. Benson, A multimaterial Eulerian formulation for the efficient solution of impact and penetration problems, Comput. Mech. 15 (6) (1995) 558–571.
[17] S.R. Cooper, D.J. Benson, V.F. Nesterenko, A numerical exploration of the role of void geometry on void collapse and hot spot formation in ductile materials, Int. J. Plasticity 16 (5) (2000) 525–540.
[18] H.S. Udaykumar, L. Tran, D.M. Belk, et al, An Eulerian method for computation of multimaterial impact with ENO shock-capturing and sharp interfaces, J. Comput. Phys. 186 (1) (2003) 136–177.
[19] L.B. Tran, H.S. Udaykumar, A particle-level set-based sharp interface Cartesian grid method for impact, penetration, and void collapse, J. Comput. Phys. 193 (2) (2004) 469–510.
[20] D. Enright, R. Fedkiw, J. Ferziger, et al, A hybrid particle level set method for improved interface capturing, J. Comput. Phys. 183 (1) (2002) 83–116.
[21] S. Osher, J.A. Sethian, Fronts propagating with curvature-dependent speed: algorithms based on Hamilton–Jacobi formulations, J. Comput. Phys. 79 (1988) 12–49.
[22] S. Osher, R.P. Fedkiw, Level set methods: an overview and some recent results, J. Comput. Phys. 169 (2) (2001) 463–502.
[23] M. Stolarska, D.L. Chopp, N. Moes, et al, Modelling crack growth by level sets in the extended finite element method, Int. J. Numer. Meth. Eng. 51 (8) (2001) 943–960.
[24] M. Duflot, A study of the representation of cracks with level sets, Int. J. Numer. Meth. Eng. 70 (11) (2007) 1261–1302.
[25] S.C. Chang, The method of space-time conservation element and solution element – a new approach for solving the Navier–Stokes and Euler equations, J. Comput. Phys. 119 (2) (1995) 295–324.
[26] S.C. Chang, X.Y. Wang, C.Y. Chow, The space-time conservation element and solution element method: a new high-resolution and genuinely multidimensional paradigm for solving conservation laws, J. Comput. Phys. 156 (1) (1999) 89–136.
[27] K.X. Liu, J.T. Wang, Analysis of high accuracy conservation-element and solution-element schemes, Chinese Phys. Lett. 21 (11) (2004) 2085–2088.
[28] C.Y. Loh, L.S. Hultgren, S.C. Chang, Wave computation in compressible flow using space-time conservation element and solution element method, AIAA J. 39 (5) (2001) 794–801.

[29] S.C. Chang, X.Y. Wang, W.M. To, Application of the space-time conservation element and solution element method to one-dimensional convection-diffusion problems, J. Comput. Phys. 165 (1) (2000) 189–215.
[30] S. Qamar, G. Warnecke, Application of space-time CE/SE method to shallow water magnetohydrodynamic equations, J. Comput. Appl. Math. 196 (1) (2006) 132–149.
[31] S. Jerez, J.V. Romero, M.D. Rosello, et al, A nonuniform mesh semi-implicit CE/SE method modelling unsteady flow in tapered ducts, Math. Comput. Simulat. 76 (1–3) (2007) 94–98.
[32] G. Wang, D.L. Zhang, K.X. Liu, An improved CE/SE scheme and its application to detonation propagation, Chinese Phys. Lett. 24 (12) (2007) 3563–3566.
[33] A.J. Torregrosa, J.R. Serrano, F.J. Arnau, et al, Experimental validation of a new semi-implicit CE/SE scheme for the calculation of unsteady one-dimensional flow in tapered ducts, Int. J. Numer. Meth. Eng. 74 (9) (2008) 1473–1494.
[34] B.S. Venkatachari, G.C. Cheng, B.K. Soni, et al, Validation and verification of courant number insensitive CE/SE method for transient viscous flow simulations, Math. Comput. Simulat. 78 (5–6) (2008) 653–670.
[35] J.T. Wang, K.X. Liu, D.L. Zhang, An improved CE/SE scheme for multi-material elastic–plastic flows and its applications, Comput. Fluids 38 (3) (2009) 544–551.
[36] D.J. Steinberg, S.G. Cochran, M.W. Guinan, A constitutive model for metals applicable at high-strain rate, J. Appl. Phys. 51 (3) (1980) 1498–1504.
[37] LS-DYNA Keyword User's Manual, version 970, Livermore Software Technology Corporation, 2003.
[38] T.H. Antoun, L. Seaman, D.R. Curran, Dynamic failure of materials, Compilation of Russian Spall Data, vol. 2, 1998.
[39] M.L. Wilkins, Computer Simulation of Dynamic Phenomena, Springer, Berlin, 1999.
[40] J.P. Ponthot, Unified stress update algorithms for the numerical simulation of large deformation elasto-plastic and elasto-viscoplastic processes, Int. J. Plasticity 18 (1) (2002) 91–126.
[41] G.R. Johnson, W.H. Cook, A constitutive model and data for metals subjected to large strains, high-strain rates and high temperatures, in: Proceedings of the 7th International Symposium on Ballistics, The Hague, The Netherlands, 1983.
[42] G.R. Johnson, W.H. Cook, Fracture characteristics of 3 metals subjected to various strains, strain rates, temperatures and pressures, Eng. Fract. Mech. 21 (1) (1985) 31–48.
[43] G.T. Camacho, M. Ortiz, Adaptive Lagrangian modelling of ballistic penetration of metallic targets, Comput. Meth. Appl. Mech. Eng. 142 (3–4) (1997) 269–301.
[44] D. Adalsteinsson, J.A. Sethian, A fast level set method for propagating interfaces, J. Comput. Phys. 118 (2) (1995) 269–277.
[45] D.P. Peng, B. Merriman, S. Osher, et al, A PDE-based fast local level set method, J. Comput. Phys. 155 (2) (1999) 410–438.
[46] M. Sussman, P. Smereka, S. Osher, A level set approach for computing solutions to incompressible 2-phase flow, J. Comput. Phys. 114 (1) (1994) 146–159.
[47] P. Smereka, Spiral crystal growth, Physica D 138 (3–4) (2000) 282–301.
[48] S.Y. Leung, H.K. Zhao, A grid based particle method for evolution of open curves and surfaces, J. Comput. Phys. 228 (20) (2009) 7706–7728.
[49] J. Eftis, J.A. Nemes, Constitutive modeling of spall fracture, Arch. Mech. 43 (2–3) (1991) 399–435.
[50] R.P. Fedkiw, T. Aslam, B. Merriman, et al, A non-oscillatory Eulerian approach to interfaces in multimaterial flows (the ghost fluid method), J. Comput. Phys. 152 (2) (1999) 457–492.
[51] F. Llorca, G. Roy. Metallurgical investigation of dynamic damage in tantalum, in: 13th APS Topical Conference on Shock Compression of Condensed Matter, APS, Portland, OR, USA, 2003.